CHAPTER 5

STUDY OF THE PLASMA X-RAY EMISSION

In the previous chapter it is shown that for the operation of the vacuum spark system with cathode aperture of 4 mm and inter-electrode spacing of 2 mm, intense emission of plasma x-ray is obtained consistently. The x-ray emission also occurs at or near the current maximum.

Using this setup, a study of the plasma x-ray emission is carried out and the results are presented in this chapter. The plasma parameters are deduced from the relative and absolute measurements of the plasma x-ray emission. From these values, the emitted radiation power and total x-ray energy are calculated. The experimental arrangements for monitoring the plasma x-ray emission are as described in Chapter 3.

5.1 : Determination of plasma parameters

5.1.1 : Determination of electron temperature using the two-foil absorption method

This technique was first proposed by Jahoda et. al. *[1960]* and has been widely used by various workers *[Ahmed & Key, 1972] [Donaldson et. al., 1973] [Pepin et. al., 1977]*. In principle, the electron temperature can be determined from an absolute measurement of bremsstrahlung transmission through two sets of absorbers. However, the relative measurements would give a more accurate value than the absolute measurements at high temperatures *[Donaldson, 1978]*. Also, in

the relative method, the electron temperature would be independent of the plasma density.

The PIN diode filters used in this work are: (i) 10 μm Cu + 24 μm aluminized mylar, (ii) 3146.8 μm mylar inclusive of 24 μm aluminized mylar and (iii) 391.6 μm mylar inclusive of 24 μm aluminized mylar. The thin and thick mylar foil combinations are chosen such that they are on either side of the Cu *K*-edge. These are shown in Figure 5.1.

From Chapter 3, the total intensity of x-ray emission detected by a PIN diode is given by

$$I = \frac{A}{4\pi d^2} \int_0^\infty P(\lambda)S(\lambda)T(\lambda)\ d\lambda \qquad A/cm^3 \qquad (5.1)$$

where A is the effective detection area and d is the distance between the plasma source and the detector. $S(\lambda)$ is the PIN diode sensitivity, $T(\lambda)$ is the transmission through the foils used and $P(\lambda)$ is the rate of energy emission per unit volume per unit wavelength of the source.

The x-ray emission from a plasma source is due to free-free, free-bound and bound-bound transitions, that is (See Section 3.7),

$$P(\lambda) = P_{ff}(\lambda) + P_{fb}(\lambda) + P_{bb}(\lambda) \qquad (5.2)$$

where $P(\lambda)$ is the total rate of emission energy, $P_{ff}(\lambda)$ is the rate of emission energy for bremsstrahlung radiation, $P_{fb}(\lambda)$ is the rate of emission energy for recombination radiation and $P_{bb}(\lambda)$ is the rate of emission energy for characteristic line radiation.

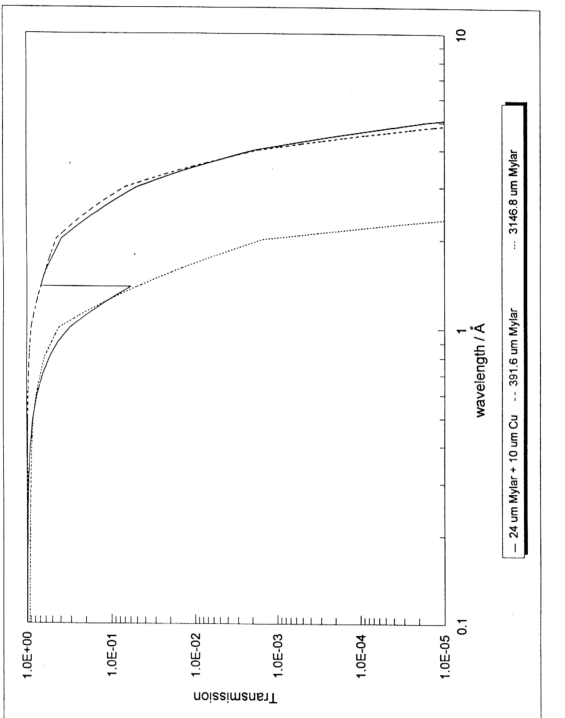

Fig. 5.1 : The transmission curves for PIN diode filters.

The line radiation is not considered because in the foil absorption technique, only the continuum radiation is considered. Since the temperature dependence of the recombination and bremsstrahlung radiation are nearly identical, the total rate of energy emission is assumed to be a multiple of the bremsstrahlung radiation, which is,

$$P(\lambda) = cP_{ff}(\lambda) \qquad W/cm^3.\text{Å} \tag{5.3}$$

where c is a factor depending on the electron temperature. However, this factor would be cancelled when the ratio of intensities transmitted through two sets of absorbers is calculated.

The ratio of the intensities detected by two PIN diodes separately filtered with foils of mass absorption coefficients μ_1 and μ_2 is given by,

$$R = \frac{I_1}{I_2} \tag{5.4}$$

where I_1 and I_2 are intensities transmitted by filters 1 and 2 respectively. For the three foil setups used, the ratios are calculated for electron temperatures of 100 eV to 10 keV. These curves are plotted in Figure 5.2. *R1* is the ratio of the output signals of 10 μm Cu + 24 μm aluminized mylar to 3146.8 μm. *R2* corresponds to the ratio of 391.6 μm mylar to 3146.8 μm mylar and *R3* is the ratio of *R1* to *R2* that is the ratio of 10 μm Cu + 24 μm aluminized mylar to 391.6 μm mylar.

The profile of curves *R1* and *R2* are similar and close to each other. *R1* and *R2* are sensitive to variation in electron temperature, however, *R*3 is not, particularly at high T_e. Therefore, the determination of electron temperature is

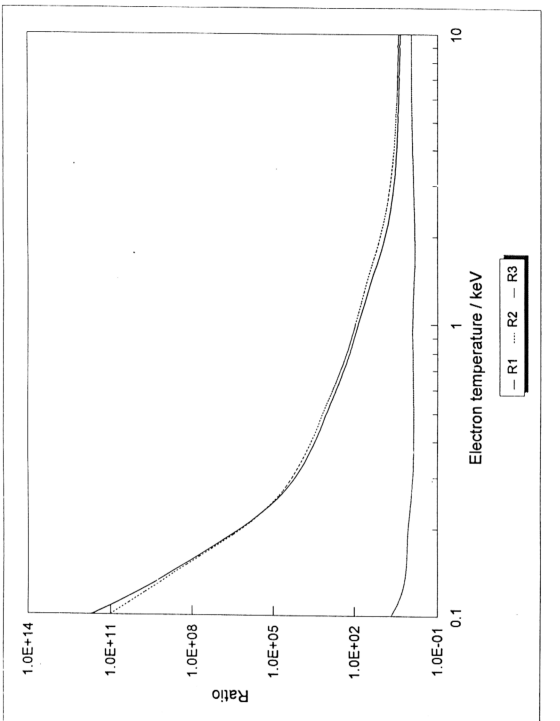

Fig. 5.2 : The graph of PIN diode ratios as a function of electron temperature, T_e.

based on the average values of *R1* and *R2*.

The ratios of PIN diode output for Cu *K* lines *[Bearden, 1967]* are calculated and plotted in Figure 5.3. The ratios of the PIN diode signals from some shots are also plotted on the same graph. If there are contributions from line radiation, the experimental values would be equal to or greater than the calculated values. Furthermore, if there are strong emission of line and continuum, the values of *R1* and *R2* would be inconsistent. The value of *R3* would also be close to 1 if line emission is dominant. Therefore, it can be concluded that the emission of plasma x-ray is dominated by the continuum radiation for the vacuum spark plasma used in this thesis.

5.1.2 : Estimation of electron density

The electron density is estimated using the hot spot diameters and PIN diode outputs. From the absolute measurement of the PIN diode signal, information such as the plasma lifetime and the detected emission energy are obtained. The plasma lifetime is taken as the FWHM of the x-ray pulse detected by the PIN diode while the area under the PIN diode output signal is used to calculate the emission energy. The calculated emission energy is then corrected for solid angle. The effective nuclear charge had to be obtained, too. An ionization model is used to determine this value. The corona model is used and this is given in section 5.2. For the estimated electron temperatures, it is found that the abundant ion species is Cu^{27+}. Therefore, the effective nuclear charge, Z_{eff}, is 27. Using these values, the electron density is calculated from the

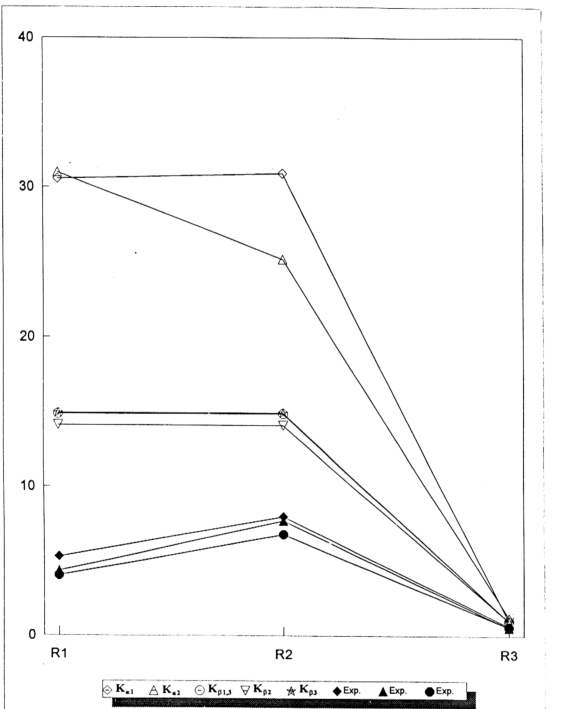

Fig. 5.3 : The graph of PIN diode ratios for Cu K lines.

following equation,

$$n_e^2 = \frac{E_m}{1.9\times10^{-28} \times \times Z_{eff} \times K \times Vol. \times t \times V} \qquad (5.5)$$

where E_m is the energy measured by the PIN diode (corrrected for solid angle) in joules, *Vol.* is the plasma volume, t is the plasma lifetime, V is the output voltage of the PIN diode and Z_{eff} is the effective nuclear charge. K is the numerically integrated value for the product of λ and T_e terms of $P_{ff}(\lambda)$, the sensitivity of PIN diode, $S(\lambda)$, and the transmission of the foil(s), $T(\lambda)$, and is given by,

$$K = \int_0^\infty \frac{\exp(-\frac{12431}{\lambda T_e})}{T_e^{1/2}\lambda^2} S(\lambda)\ T(\lambda)\ d\lambda \qquad A/cm^3 \qquad (5.6)$$

5.1.3 : Calculation of emission spectrum and the total energy emitted

Using the plasma parameters obtained from the experiments, the bremsstrahlung emission spectrum given in equation (3.10) is calculated. By substituting the ion density with n_e/Z_{eff}, equation (3.10) becomes,

$$P_{ff}(\lambda) = 1.9\times10^{-28} \frac{n_e^2 Z_{eff}}{T_e^{1/2}\lambda^2} \exp(-\frac{12431}{\lambda T_e}) \qquad W/cm^3 \qquad (5.7)$$

The total rate of energy emitted is calculated by integrating equation (5.7) over all wavelengths and multiplying this value with the plasma volume. The total

energy is then calculated by taking the product of the total rate of energy emitted and the plasma lifetime.

5.2 : The steady-state corona model

The corona model was proposed to explain some features of the spectrum of the solar corona. This model has also been found useful in discussing low density laboratory plasmas. The coronal model is valid if the electron density is *[McWhirter, 1965]* :

$$n_e < 10^{16} T_e^{7/2} \qquad (5.8)$$

where n_e is the electron density in cm^{-3} and T_e is the electron temperature in eV. However, certain assumptions are made in using this model to explain the features of low density laboratory plasmas, which are *[McWhirther, 1965]* :

(i) The plasma is optically thin, that is, the emitted radiation is not reabsorbed by the plasma.

(ii) The electrons of the plasma have a Maxwellian distribution.

(iii) At sufficiently low electron densities, the rate of radiative recombination $[\, e + A(z+1) \rightarrow A(z) + h\nu \,]$ is more important than the three-body recombination $[\, e + N(z) \rightarrow N(z+1) + e + e \,]$.

(iv) The change in the plasma parameters takes place sufficiently slowly for the population densities to take up their new steady-state values at each instant.

(v) There are only negligible number of ions in their excited levels compared with the ground level.

(vi) The ratio of $\chi(z, g)/ kT_e$, as required by the steady-state corona model, must be between 1 to 10, where $\chi(z, g)$ is the ionization potential of ion at charge state z in ground level g.

Since there are negligible numbers of ions at excited level, the plasma is in an equilibrium between ionization and recombination. This can be expressed as:

$$n_e n_i(z,g) S(T_e,z,g) = n_e n_i(z+1,g)\,\alpha(T_e,z+1,g) \tag{5.9}$$

that is,

$$\frac{n_i(z+1,g)}{n_i(z,g)} = \frac{S(T_e,z,g)}{\alpha(T_e,z+1,g)} \tag{5.10}$$

where $S(T_e, z, g)$ is the collisional ionization coefficient and $\alpha(T_e, z+1, g)$ is the radiative recombination coefficient. The ratio between consecutive ions in a corona model plasma given by equation (5.10), thus shows that the distribution of ions is independent of electron density.

The collisional ionization coefficient, $S(T_e, z, g)$, is given by Burgess *[1961]* as,

$$S(T_e,z,g) = 2.34\times10^{-7}\,\frac{\zeta T_e^{1/4}}{\chi(z,g)^{7/4}}\exp[-\frac{\chi(z,g)}{kT_e}] \qquad cm^3 s^{-1} \tag{5.11}$$

where ζ is the number of outer electrons ($\zeta = 1$ for hydrogen and hydrogen-like

ions and so on), T_e is in °K and χ is in eV, while, the radiative recombination coefficient, $\alpha(T_e, z, g)$, given by Seaton *[1959]* with a slight modification by McWhirter *[1965]* is

$$\alpha(T_e, z, g) = \frac{2.05\times10^{-12}\chi(z-1,g)}{T_e^{1/2}} \qquad cm^3 s^{-1} \tag{5.12}$$

Substituting equation (5.11) and (5.12) in equation (5.10) gives the ratio between consecutive ions as

$$\frac{n_i(z+1,g)}{n_i(z,g)} = 1.27\times10^8 \frac{\zeta T_e^{3/4}}{\chi(z,g)^{11/4}} \exp[-\frac{\chi(z,g)}{T_e}] \tag{5.13}$$

where T_e and $\chi(z, g)$ are in eV.

For a particular electron temperature, T_e, let the ionization fraction $\alpha_z = n_i(z, g)/n_t$ where n_t is the total particle number density of the plasma. Let f_z, the steady state ratio between consecutive ions be equal to $n_i(z+1, g)/n_i(z, g)$ which is expressed by equation (5.13). Therefore,

$$\alpha_{z+1} = \alpha_z f_z \tag{5.14}$$

Since,

$$\sum_{z=0}^{A} \alpha_z = 1 \tag{5.15}$$

and α_0 is

$$\alpha_0 = \frac{1}{1+S_1} \tag{5.16}$$

with S_1 given by :

$$S_1 = f_0 + f_0 f_1 + f_0 f_1 f_2 + \ldots + \prod_{z=0}^{z=A-1} f_z \qquad (5.17)$$

where A is the atomic number. Thus the values of α_z (from $z = 1$ to A) can be evaluated using equation (5.14). The graph of α_z versus T_e for electron temperatures of 100 eV to 10 keV is plotted and shown in Figure 5.4. From this graph, it can be seen that at temperatures between 1 to 10 keV the abundant species are Cu^{27+}. The ionization potentials used in these calculations are taken from Lide *[1992-93]*.

The effective nuclear charge, Z_{eff}, is then determined using the following relation:

$$Z_{eff} = \frac{\sum_{z=1}^{z=A} \alpha_z z^2}{\sum_{z=0}^{z=A} \alpha_z z} \qquad (5.17)$$

The graph of Z_{eff} as a function of T_e is plotted and shown in Figure 5.5. From this graph, the effective nuclear charge, Z_{eff}, for a copper plasma at temperature between 1 to 10 keV is approximately 27.

5.3 : X-ray emission from the vacuum spark discharge

Generally, there are two types of x-ray emission observed in a vacuum spark discharge. One is characterised by early emission of x-ray before or during

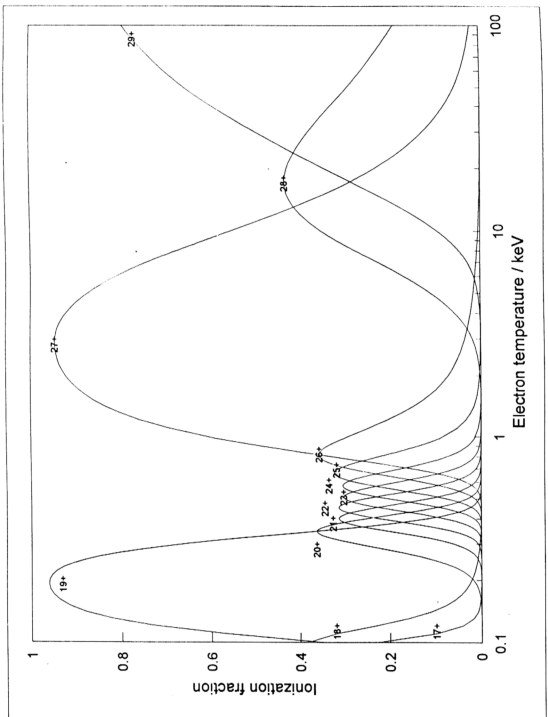

Fig. 5.4 : The graph of ionization fraction as a function of electron temperature, T_e.

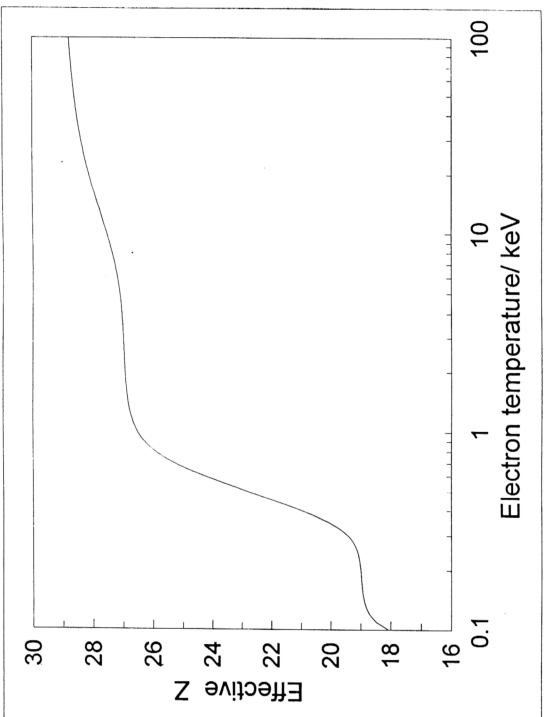

Fig. 5.5 : The graph of effective nuclear charge, Z_{eff}, as a function of electron temperature, T_e.

the start of the breakdown. This type of emission is due to the beam-target interaction. The other type is emission of x-ray from plasma formed from the anode material. This occurs about 100 ns after the start of the breakdown.

In Figures 5.6 and 5.7 are shown discharges emitting beam-target x-rays. This type of emission is similar to the x-rays emitted from conventional electron impact sources. The x-rays emitted before the breakdown are due to the electron beam generated from the transient hollow cathode effect.

In Figure 5.6, a point-like emission is observed at the tip of the anode. This can be attributed to a well-collimated, on-axis beam of electrons bombarding the anode. And in Figure 5.7, the x-ray emission observed along the anode stem is probably due to currents flowing from the anode stem.

There are many variations in the formation of plasma as seen from the pinhole images. In Figure 5.8 is shown a discharge in which the hot spot is very distinct and appears at the top of the plasma cloud. The pre-breakdown and secondary electron beams are weak therefore not observed. Both the soft and hard x-ray signals are detected. In this discharge the hot spot is formed close to the cathode. However, the location of the hot spot does not determine the characteristics of the x-ray emission. This can be seen in Figure 5.9 in which the hot spot is formed near the anode. The x-ray signals detected are similar as in the previous discharge. The difference in this discharge compared to the previous one is that there are x-ray emissions due to pre-breakdown and secondary electron beams.

Some discharges also display similar hard x-ray emission but with very weak or no emission of soft x-ray. A typical discharge of this nature is shown

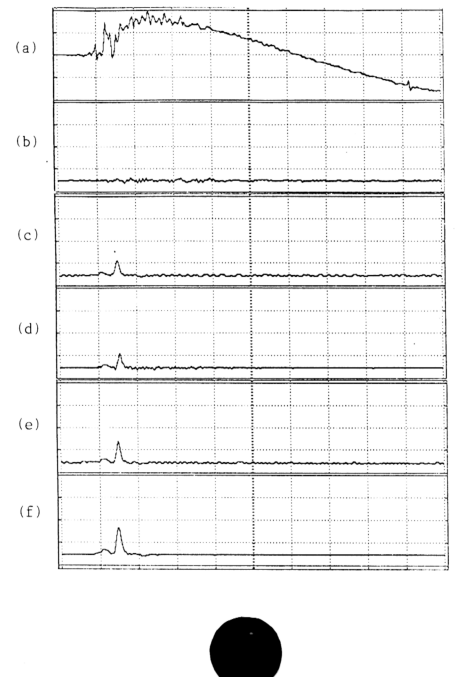

Fig. 5.6 : Oscilloscope signals for the vacuum spark discharge without hot spot formation. The corresponding pinhole image is shown. Magnification ~ 1.47. Shot #9412009, PH 4 : #3. (Time-base : 100 ns/div.).
(a) *dI/dt*, 10 V/div. **(b)** XRD (2.5 μm aluminized mylar), 1 V/div.
(c) PIN 1 (10 μm Cu + 24 μm aluminized mylar), 8 V/div.
(d) PIN 2 (3146.8 μm mylar), 2 V/div. **(e)** PIN 3 (391.6 μm mylar), 8 V/div.
(f) Side-on PIN (36 μm aluminized mylar), 50 V/div.

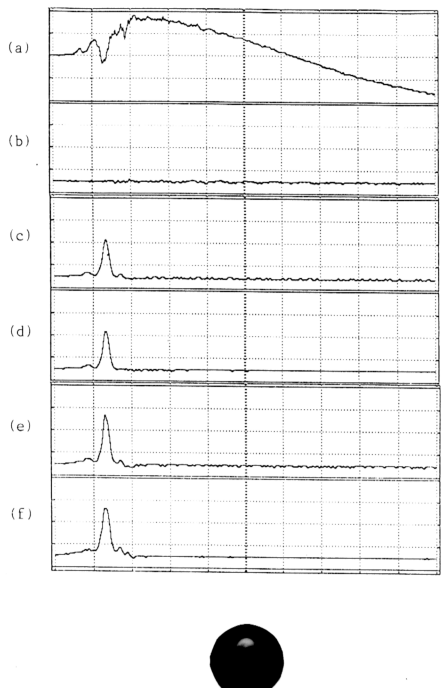

Fig. 5.7 : Oscilloscope signals for the vacuum spark discharge without hot spot formation. The corresponding pinhole image is shown. Magnification ~ 1.47. Shot #9501081, PH 38 : #3. (Time-base : 100 ns/div.).
(a) *dI/dt*, 10 V/div. **(b)** XRD (2.5 μm aluminized mylar), 1 V/div.
(c) PIN 1 (10 μm Cu + 24 μm aluminized mylar), 8 V/div.
(d) PIN 2 (3146.8 μm mylar), 2 V/div. **(e)** PIN 3 (391.6 μm mylar), 8 V/div.
(f) Side-on PIN (36 μm aluminized mylar), 50 V/div.

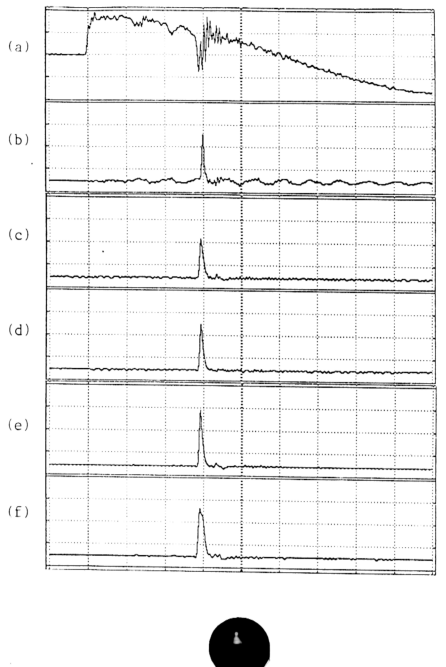

Fig. 5.8 : Oscilloscope signals for the vacuum spark discharge with hot spot formation. The corresponding pinhole image is shown. Magnification ~ 1.47.
Shot #9501008, PH 22 : #1. (Time-base : 100 ns/div.).
(a) *dI/dt*, 10 V/div. **(b)** XRD (2.5 μm aluminized mylar), 1 V/div.
(c) PIN 1 (10 μm Cu + 24 μm aluminized mylar), 8 V/div.
(d) PIN 2 (3146.8 μm mylar), 2 V/div. **(e)** PIN 3 (391.6 μm mylar), 8 V/div.
(f) Side-on PIN (36 μm aluminized mylar), 50 V/div.

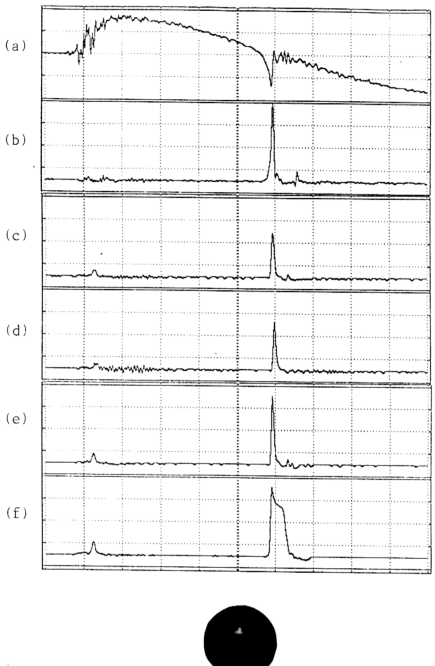

Fig. 5.9 : Oscilloscope signals for the vacuum spark discharge with hot spot formation. The corresponding pinhole image is shown. Magnification ~ 1.47.
Shot #9412055, PH 15 : #1. (Time-base : 100 ns/div.).
(a) *dI/dt*, 10 V/div. **(b)** XRD (2.5 μm aluminized mylar), 1 V/div.
(c) PIN 1 (10 μm Cu + 24 μm aluminized mylar), 8 V/div.
(d) PIN 2 (3146.8 μm mylar), 2 V/div. **(e)** PIN 3 (391.6 μm mylar), 8 V/div.
(f) Side-on PIN (36 μm aluminized mylar), 50 V/div.

in Figure 5.10. The pinhole image shows only a diffused plasma cloud. There is no hot spot image as seen in the previous discharges. On the other hand, discharges with strong soft x-ray emission but with weak hard x-ray emission show faint hot spot image in the pinhole images. This is shown in Figure 5.11.

In some discharges with very strong emission of hard x-ray, fluorescence radiation from the cathode is observed. This is shown in Figure 5.12. Soft x-rays are emitted, however, there are no hot spots observed, probably obscured by the expanding plasma.

Based on the pinhole images and the time-resolved x-ray detection, an explanation on the relationship between hard and soft x-ray emission on the formation of hot spots is given as follows. Emission of hard x-rays does not necessarily mean that hot spots are formed. This is evident from some discharges where hard x-rays are emitted but the pinhole images do not show any hot spot image. On the other hand, discharges with strong soft x-ray emission (strong XRD signal) but with weak hard x-ray emission show images of small diffused hot spots. From these observations, it can be assumed that the formation of hot spots is signified by emission of soft x-rays, which is consistent with results published in the literature.

The emissions of hard x-rays are probably the result of turbulence or instabilities occurring during the conducting period. This is evident in Figure 5.10 where there are no soft x-ray emissions but hard x-rays are still emitted and the dI/dt signal shows a disruption in the current flow. A possible explanation would be that a sudden change in the current flow would induce very high transient voltages that in turn would accelerate the charges. The electron beam thus formed

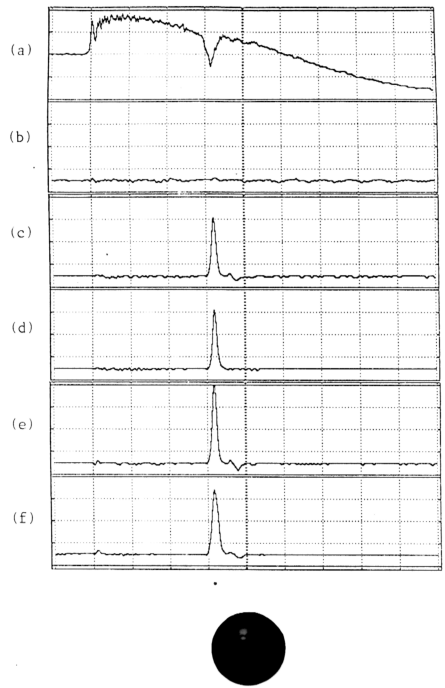

Fig. 5.10 : Oscilloscope signals for the vacuum spark discharge without hot spot formation. The corresponding pinhole image is shown. Magnification ~ 1.47. Shot #9501047, PH 31 : #1. (Time-base : 100 ns/div.).
(a) *dI/dt*, 10 V/div. **(b)** XRD (2.5 μm aluminized mylar), 1 V/div.
(c) PIN 1 (10 μm Cu + 24 μm aluminized mylar), 8 V/div.
(d) PIN 2 (3146.8 μm mylar), 2 V/div. **(e)** PIN 3 (391.6 μm mylar), 8 V/div.
(f) Side-on PIN (36 μm aluminized mylar), 50 V/div.

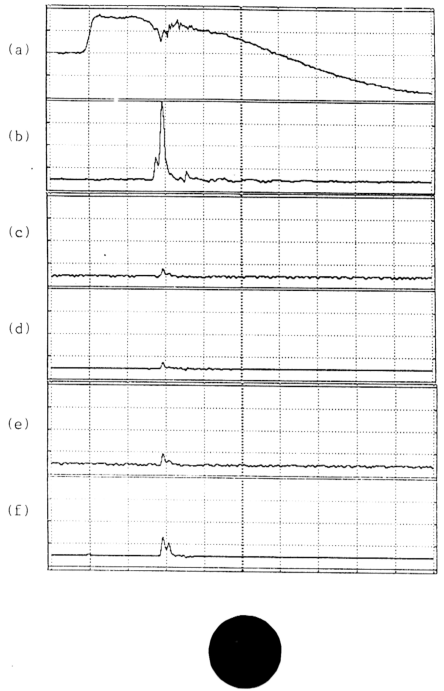

Fig. 5.11 : Oscilloscope signals for the vacuum spark discharge with hot spot formation. The corresponding pinhole image is shown. Magnification ~ 1.47. Shot #9501053, PH 32 : #2. (Time-base : 100 ns/div.).
(a) *dI/dt*, 10 V/div. **(b)** XRD (2.5 μm aluminized mylar), 1 V/div.
(c) PIN 1 (10 μm Cu + 24 μm aluminized mylar), 8 V/div.
(d) PIN 2 (3146.8 μm mylar), 2 V/div. **(e)** PIN 3 (391.6 μm mylar), 8 V/div.
(f) Side-on PIN (36 μm aluminized mylar), 50 V/div.

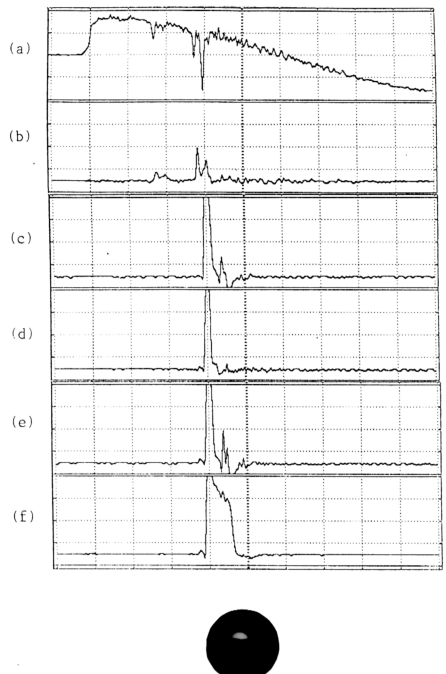

Fig. 5.12 : Oscilloscope signals for the vacuum spark discharge with hot spot formation. The corresponding pinhole image is shown. Magnification ~ 1.47.
Shot #9501037, PH 28 : #4. (Time-base : 100 ns/div.).
(a) *dI/dt*, 10 V/div. **(b)** XRD (2.5 μm aluminized mylar), 1 V/div.
(c) PIN 1 (10 μm Cu + 24 μm aluminized mylar), 8 V/div.
(d) PIN 2 (3146.8 μm mylar), 2 V/div. **(e)** PIN 3 (391.6 μm mylar), 8 V/div.
(f) Side-on PIN (36 μm aluminized mylar), 50 V/div.

interacts with the dense plasma and emits hard x-ray.

5.4 : Estimation of hot spot diameter and electron density

Using the method described in 3.4.2, the diameters of the hot spot is estimated. The discharges from which the hot spot diameter is estimated are shown in Figures 5.13 to 5.16. The results are given in Table 5.1 with the corresponding electron temperatures. The diameters of the hot spot ranges from 100 - 200 μm. Estimation of the hot spot diameter from the pinhole image give values between 250 - 350 μm. Since the hot spot diameter estimated from the slit-wire camera is taken to be a more accurate estimate of the hot spot size, the diameter of the hot spot is taken to be between 100 - 200 μm.

Shot #	T_e / keV	diameter / μm	radius / μm	Vol. / cm^3
9501010	2.8	203.2	101.6	4.4×10^{-6}
9501023	2.4	116.87	58.435	8.4×10^{-7}
9501026	2.6	158.18	79.09	2.1×10^{-6}
9501036	2.7	113.14	56.57	7.6×10^{-7}

Table 5.1

However, this estimate does not preclude the existence of smaller structures of hot spots. This is because the slit-wire camera's image is time-integrated and if smaller structures exist, they would be obscured by the expanding plasma.

Using the estimated hot spot diameters and the PIN diode output, the

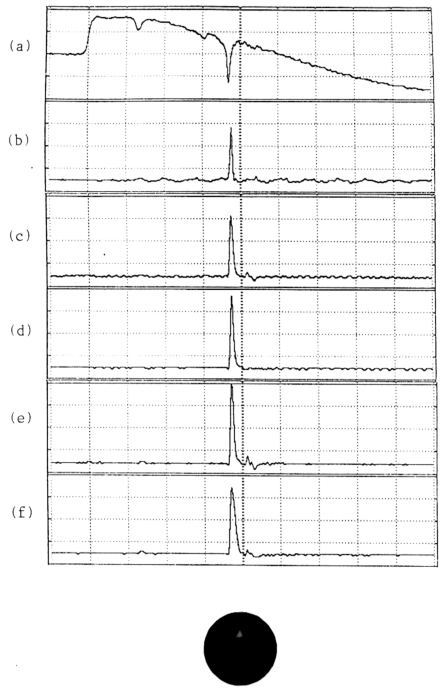

Fig. 5.13 : Oscilloscope signals for the vacuum spark discharge with hot spot formation. The corresponding pinhole image is shown. Magnification ~ 1.47.
Shot #9501010, PH 23 : #2. (Time-base : 100 ns/div.).
(a) *dI/dt*, 10 V/div. **(b)** XRD (2.5 μm aluminized mylar), 1 V/div.
(c) PIN 1 (10 μm Cu + 24 μm aluminized mylar), 8 V/div.
(d) PIN 2 (3146.8 μm mylar), 2 V/div. **(e)** PIN 3 (391.6 μm mylar), 8 V/div.
(f) Side-on PIN (36 μm aluminized mylar), 50 V/div.

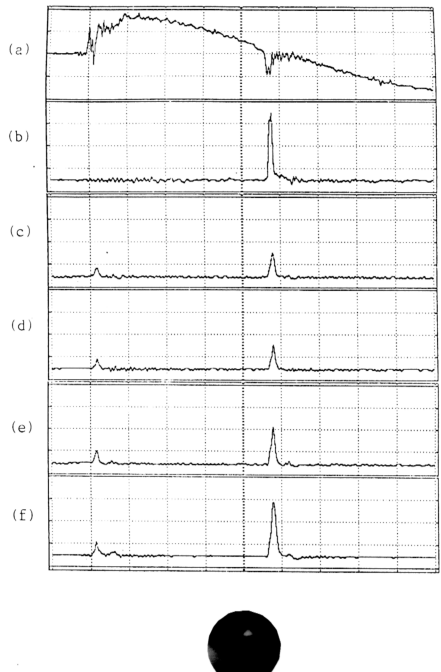

Fig. 5.14 : Oscilloscope signals for the vacuum spark discharge with hot spot formation. The corresponding pinhole image is shown. Magnification ~ 1.47.
Shot #9501023, PH 25 : #5. (Time-base : 100 ns/div.).
(a) *dI/dt*, 10 V/div. **(b)** XRD (2.5 μm aluminized mylar), 1 V/div.
(c) PIN 1 (10 μm Cu + 24 μm aluminized mylar), 8 V/div.
(d) PIN 2 (3146.8 μm mylar), 2 V/div. **(e)** PIN 3 (391.6 μm mylar), 8 V/div.
(f) Side-on PIN (36 μm aluminized mylar), 50 V/div.

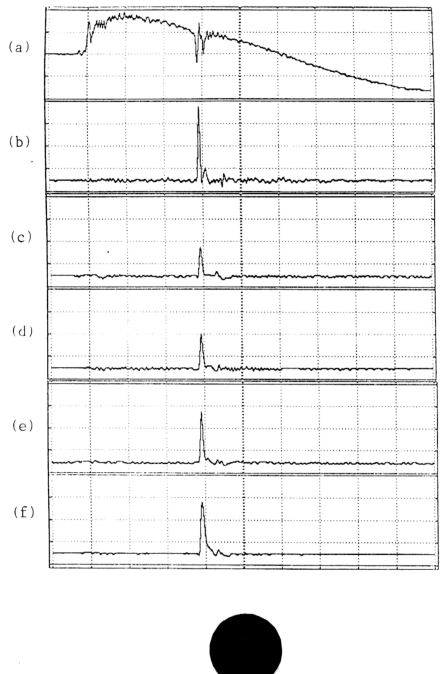

Fig. 5.15 : Oscilloscope signals for the vacuum spark discharge with hot spot formation. The corresponding pinhole image is shown. Magnification ~ 1.47.
Shot #9501026, PH 26 : #3. (Time-base : 100 ns/div.).
(a) *dI/dt*, 10 V/div. **(b)** XRD (2.5 μm aluminized mylar), 1 V/div.
(c) PIN 1 (10 μm Cu + 24 μm aluminized mylar), 8 V/div.
(d) PIN 2 (3146.8 μm mylar), 2 V/div. **(e)** PIN 3 (391.6 μm mylar), 8 V/div.
(f) Side-on PIN (36 μm aluminized mylar), 50 V/div.

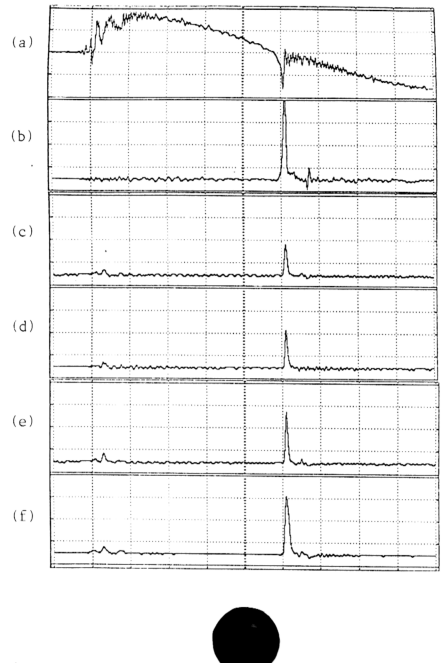

Fig. 5.16 : Oscilloscope signals for the vacuum spark discharge with hot spot formation. The corresponding pinhole image is shown. Magnification ~ 1.47.
Shot #9501036, PH 28 : #3. (Time-base : 100 ns/div.).
(a) dI/dt, 10 V/div. **(b)** XRD (2.5 μm aluminized mylar), 1 V/div.
(c) PIN 1 (10 μm Cu + 24 μm aluminized mylar), 8 V/div.
(d) PIN 2 (3146.8 μm mylar), 2 V/div. **(e)** PIN 3 (391.6 μm mylar), 8 V/div.
(f) Side-on PIN (36 μm aluminized mylar), 50 V/div.

electron density is calculated using equation (5.5). The calculated electron densities obtained for each PIN diode are shown in Table 5.2.

		n_e / cm^{-3}		
Shot. #	T_e / keV	PIN 1	PIN 2	PIN 3
9501010	2.8	5.4×10^{20}	4.7×10^{20}	-
9501023	2.4	9.6×10^{20}	8.3×10^{20}	9.8×10^{20}
9501026	2.6	6.0×10^{20}	5.4×10^{20}	6.7×10^{20}
9501036	2.7	9.6×10^{20}	8.7×10^{20}	1.1×10^{21}

Table 5.2

The electron densities range between 4.7×10^{20} - 1.1×10^{21} cm^{-3}. Using these values, the total energy and power emitted are calculated. These are given in the following section.

5.5 : Calculated emission power and energy

By substituting the estimated values of electron temperature, hot spot size and electron density, the total emitted power and energy are calculated as described in section 5.1.3. The results of these calculations are shown in Table 5.3. These are average values taken from the PIN diodes.

For the corresponding electron temperature and density of the hot spot deduced from the PIN diode response, the total emission power per unit volume is between (1.4 - 5.2) $\times 10^{11}$ W cm^{-3}, the total emission power is between (4.0 - 6.2) $\times 10^{5}$ W and the total emission energy is between (2.9 - 5.6) $\times 10^{-3}$ J.

Shot #	< P / V > (W cm^{-3})	< P > (W)	< E > (J)
9501010	1.4×10^{11}	6.2×10^{5}	5.6×10^{-3}
9501023	4.4×10^{11}	3.7×10^{5}	3.6×10^{-3}
9501026	2.0×10^{11}	4.1×10^{5}	3.0×10^{-3}
9501036	5.2×10^{11}	4.0×10^{5}	2.9×10^{-3}

Table 5.3

5.6 : Spectral analysis of the discharge

The spectrograph obtained using the mica crystal convex spectrometer (Sec. 3.5) is shown in Figure 5.17. The film is exposed to a total of 20 discharges. Due to the geometrical arrangement used in this work, only the higher order diffraction lines are obtained. From the X vs α graph (See Fig. 3.13), the lines are identified as K_α lines of orders 2, 3 and 4. Some lines could not be identified, probably due to the bending of the crystal and the spatial variation of the point of emission from shot to shot. The left portion of the film is caused by direct exposure to the continuum radiation.

From the spectrograph, it can be observed that the emission from the vacuum spark is a mixture of continuous spectrum and characteristic lines. The emission of *K*-shell lines can be related to the existence of highly ionized state of the atoms of the electrode material. Theoretically it is predicted that the K line radiation starts at a temperature $T_K(Z_n)$ that depends on the nuclear charge Z_n. This temperature is approximately $T_K \approx 3 \times 10^{-3} Z_n^4$ eV *[Breton et. al., 1978]*. For copper, this temperature would be about 2.1 keV. In this work, the estimated

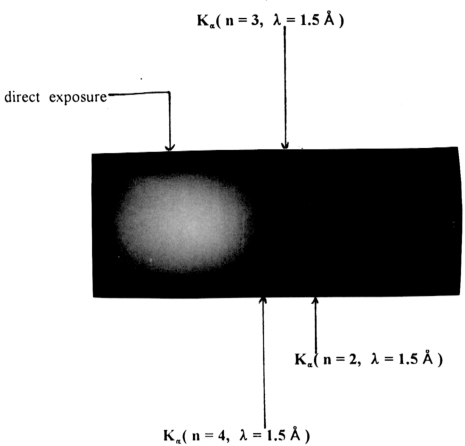

Fig. 5.17 : The spectrograph obtained using the mica crystal convex spectrometer.

electron temperatures are ≥2.0 keV, therefore *K*-shell line radiation would be emitted. However, the intensity of the line radiation is low compared to the bremsstrahlung radiation. According to Koshelev & Pereira *[1991]*, the maximum atomic number for which the *K* shell can be reached is $Z_{max} \approx 70 \times I^{1/2}$ where *I* is the pinch current in MA. Assuming that the pinch current is equal to the peak current, 126 kA, this formula gives $Z_n \leq 25$ for He-like ions to be excited in a micropinch. Therefore, for the copper ($Z_n = 29$) pinch the *K* lines are weak. For the present setup, strong emission of *K* lines from copper plasma can be observed if the pinch current is greater than 0.17 MA.